Discrete control for state of charge balance in DC microgrids considering the disturbance of photovoltaics

Boxi Li [a], Tao Huang [b,*], Zhengmin Kong [a], Lei Chen [a,*], Jiajia Yang [c], Shikuan Sun [a]

[a] School of Electrical Engineering and Automation, Wuhan University, Wuhan 430072, Hubei, China
[b] College of Science and Engineering, James Cook University, Cairns 4878, Queensland, Australia
[c] College of Science and Engineering, James Cook University, Townsville 4811, Queensland, Australia

ARTICLE INFO

ABSTRACT

This study examines State of Charge (SoC) balancing control in DC microgrids subject to photovoltaic (PV) fluctuations, aiming to optimize power distribution in energy storage systems influenced by PV disturbances. The proposed approach enhances both the lifespan of storage systems and microgrid stability. To mitigate voltage variation due to PV perturbation, the paper introduces an adjustment in droop control offset. Additionally, it presents a novel discrete Sliding Mode Controller (SMC) characterized by reduced parameter sensitivity, thus enhancing control responsiveness. A SoC balancing control strategy employing sliding mode control is developed to equalize SoC levels across Battery Energy Storage Systems during both charge and discharge cycles. The stability of this strategy is substantiated through the construction of a Lyapunov function. Simulations conducted in a distributed DC microgrid environment using Simulink/SimPower Systems demonstrate the efficacy of the discrete SMC and the SoC balancing algorithm, achieving uniform SoC in energy storage nodes during operation, with improved robustness against PV perturbations.

1. Introduction

In the context of advancing low-carbon and environmental protection initiatives [1], microgrids have been increasingly recognized for their ability to integrate Distributed Energy Resources (DERs) [2], Battery Energy Storage Systems (BESSs), and various load types [3]. However, the power quality of microgrids is susceptible to the inherent instability and unpredictability of Renewable Energy Sources (RESs), such as wind and photovoltaic (PV) systems [4], which may induce severe voltage fluctuations at the load end or compromise the power quality of the main grid.

To address this challenge, BESSs are often employed within microgrids comprising RESs to provide a buffer against power discrepancies. When RES output falls short of load demand, BESSs discharge to compensate, and conversely, they absorb excess power when RES output exceeds demand. Nonetheless, as microgrid dimensions expand, the scaling of BESS infrastructure represents a substantial investment in microgrid development.

Islanded microgrids encounter two principal challenges that necessitate mitigation strategies. Firstly, the output of RESs is subject to environmental contingencies, leading to unpredictability. While BESSs can mitigate these fluctuations, they are not entirely effective against bus voltage variations across the microgrid. Enhancing the controllers' response speed and operational range is critical for addressing the volatility in RES output. In this regard, the significance of computer-controlled sampling time is underscored for digital controllers with discrete-time control features [5,6]. Nonlinear controllers are increasingly being adopted for their improved response times in PV-based microgrids [7]. Additionally, H_∞ theory has been acknowledged for its capacity to manage external disturbances and issues related to communication links [8]. Sliding mode control is also recognized for its robustness against operational inconsistencies in PV-based microgrids [9], with adaptive adjustment techniques for sliding mode surface parameters proposed to bolster control resilience [10]. However, the effectiveness of these controllers is contingent upon the optimization of their parameters.

Moreover, in microgrids with high RESs penetration, the equitable distribution of power among BESS nodes is imperative [11]. State of Charge (SoC) equilibrium is critical to prevent complications, as imbalances can diminish BESS longevity due to extended deep discharging or overcharging. Such anomalies can precipitate unscheduled downtimes, overburdening the remaining BESS units and leading to elevated temperatures or, in extreme cases, fires.

Various methodologies have been proposed for balancing the SoC among BESSs, encompassing power, voltage, and current control techniques. Strategies such as the adaptive power allocation described in [12], utilize consensus-based algorithms for equitable load current distribution, as elaborated in [13]. A DC bus voltage control approach using a multi-agent consensus algorithm to adjust the droop coefficient dynamically is detailed in [14]. Moreover, a power management strategy has been developed to maintain power quality for BESSs, ensuring load current stability and compensating for line impedance disparities, as reported in [3]. However, traditional control strategies may not adequately address the nonlinear dynamics of microgrids due to the variable nature of PV system outputs.

In light of these considerations, a novel nonlinear BESS model is developed in this paper to reflect the erratic nature of PV output, distinguishing it from existing models such as those referenced in [13,15]. The new BESS model captures the stochastic behavior of BESS charging and discharging states under PV perturbations, offering a more accurate representation of PV power output. A discrete Sliding Mode Controller (SMC) has been designed to respond swiftly and robustly to disturbances during PV generation, with the notable advantage of minimal parameter dependency, marking a departure from existing nonlinear controllers in [6,8,12,15]. Consequently, this controller is more adept at adapting to voltage fluctuations. A discrete observer has been integrated to reconcile voltage regulation with the SoC balancing control strategy. Finally, a novel droop control-based SoC strategy is proposed, enabling distributed BESS nodes to achieve SoC equilibrium in both charging and discharging states.

The main contributions of this paper are summarized as follows

1. A nonlinear model has been formulated, delineating the external equivalent resistance for each BESS, which more accurately characterizes the instability and unpredictability present during PV generation.
2. An enhanced droop control strategy has been proposed, aimed at attenuating voltage fluctuations due to PV perturbations.
3. A discrete SMC has been designed to improve the voltage robustness at individual BESS nodes, predicated on a PV-based nonlinear microgrid model. Conditions for the existence of the sliding mode surface have been established, thereby simplifying the accuracy of parameter settings.
4. An innovative SoC balancing control strategy, predicated on sliding mode control, has been developed. This strategy enables the attainment of SoC equilibrium across BESS units during both charge and discharge cycles in accordance with the nonlinear model. Furthermore, the cooperation of SoC under the proposed model has been validated through the construction of a Lyapunov function.

The structure of the remainder of this document is outlined as follows. Section 2 provides foundational information, including an overview of Maximum Power Point Tracking (MPPT) functionality, V-I based droop control mechanisms, and pertinent graph theory concepts. Section 3 delineates the design of a discrete SMC and details the accompanying proof procedure. In Section 4, the architecture of the distributed observer alongside the methodology for voltage regulation is presented. Subsequently, Section 5 introduces a SoC balancing control strategy and validates its stability through the formulation of a Lyapunov function. Section 6 corroborates all theoretical findings, with concluding remarks presented in Section 7.

2. Preliminary knowledge

2.1. PV and MPPT

Fig. 1 depicts a typical microgrid configuration, wherein PV is identified as a source of clean energy capable of transforming solar irradiance into electrical power. The relationship between PV output power and irradiance is demonstrated in Fig. 2(a), illustrating variable power output curves corresponding to fluctuating irradiance levels. Current research efforts are directed towards optimizing the efficiency of PVs by enabling their operation at the maximum power point of these curves, which is MPPT mode. This optimal operational point is attained by modulating the output voltage V_{dc}^{pv} of PVs to coincide with the maximum power point under diverse irradiance scenarios. The mechanism for achieving this, illustrated in Fig. 2(b), involves the manipulation of the switch K_s. Consequently, in a DC microgrid inclusive of PVs, power generation via MPPT is designed to maximize solar energy utilization despite the inherent uncertainty and variability of sunlight exposure.

2.2. Graph theory

In this study, it is posited that the graph characterizing the interconnections between BESSs, denoted as $\mathcal{G} = (\mathcal{V}, \mathcal{E}, \mathcal{A})$, is both connected and bidirectional. Here, $\mathcal{V}$ represents the set of nodes $\mathcal{V}_1, \mathcal{V}_2, \ldots, \mathcal{V}_M$, $\mathcal{E} \subseteq \mathcal{V} \times \mathcal{V}$ signifies the set of edges, and $\mathcal{A}(\mathcal{G}) = [a_{ij}]_{M \times M}$ is the adjacency matrix. An element a_{ij} of this matrix is defined by:

$$a_{ij} = \begin{cases} 1, \text{if} (\mathcal{V}_i, \mathcal{V}_j) \in \mathcal{E} \\ 0, \text{otherwise} \end{cases}. \tag{1}$$

The in-degree matrix $D(\mathcal{G})$ is subsequently defined as $D(\mathcal{G}) = diag\{d_i\} \in R^{M \times M}$, where $d_i = \sum_{j=1}^{M} a_{ij}$. The Laplacian matrix $L(\mathcal{G})$ is expressed as:

$$L(\mathcal{G}) = D(\mathcal{G}) - \mathcal{A}(\mathcal{G}) = [l_{ij}]_{M \times M}. \tag{2}$$

where the elements l_{ij} are computed according to:

$$l_{ij} = \begin{cases} -a_{ij}, & i \neq j \\ \sum_{i=1}^{M} a_{ij}, & i = j \end{cases}. \tag{3}$$

Given the bidirectional nature of the communication within the paper's scope (i.e., $a_{ij} = a_{ji}$), the graph $\mathcal{G}$ has strong connectivity property and the Laplacian matrix is required to be a real symmetric matrix.

Moreover, the directed graph corresponding to graph $\mathcal{G}$ is denoted as G. The incidence matrix for G is defined as $B(G)$. Building on the premise established in [16], the Laplacian matrix for an undirected graph $\mathcal{G}$ can be factorized into the incidence matrix $B(G)$ and its transpose $B^T(G)$, a relationship that remains invariant with respect to the direction of G, as shown in:

$$L(\mathcal{G}) = B(G)B^T(G). \tag{4}$$

2.3. Droop control

Power allocation across nodes in microgrids through droop control is achieved using distinct droop coefficients. The current droop control investigated in this paper enables equitable load sharing among BESS nodes, which is expressed as:

$$V_i^{dc,ref}(t) = v^{nom} - i_i^{bus}(t)r_i, \tag{5}$$

where $V_i^{dc,ref}$ is the reference voltage for the ith BESS, v^{nom} is the nominal set point voltage, i_i^{bus} is the output current of the converter, and r_i is the initial droop coefficient for the ith BESS. The droop coefficient r_i is proportionate to the battery capacity, defined as:

$$\frac{r_i}{r_j} = \frac{Q_j}{Q_i}. \tag{6}$$

with Q_i indicating the battery capacity in the ith BESS. The improved droop control presented in this paper uses the output current of the battery as the droop offset to counteract PV perturbations effectively. This approach simplifies the design of SMCs. The revised formula is given as:

$$V_i^{dc,ref}(t) = v^{nom} - i_i^b(t)r_i, \tag{7}$$

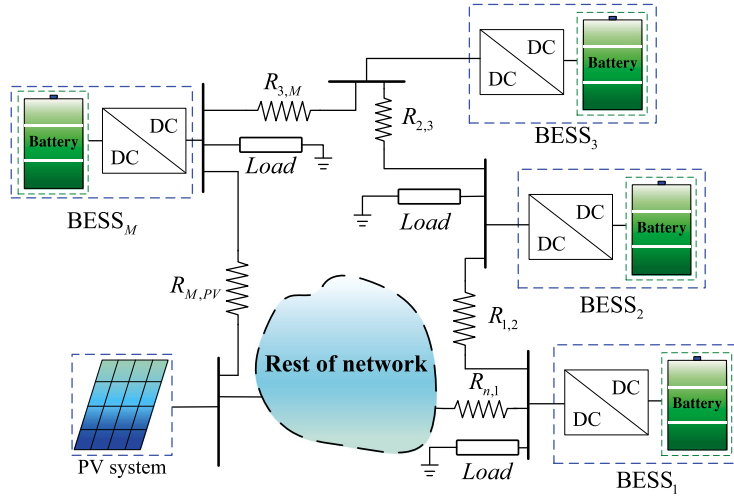where i_i^b is the battery's output current in the ith BESS.

Fig. 1. The topology of DC Microgrid.

(a) Schematic diagram of PVs power output curve under different irradiance.
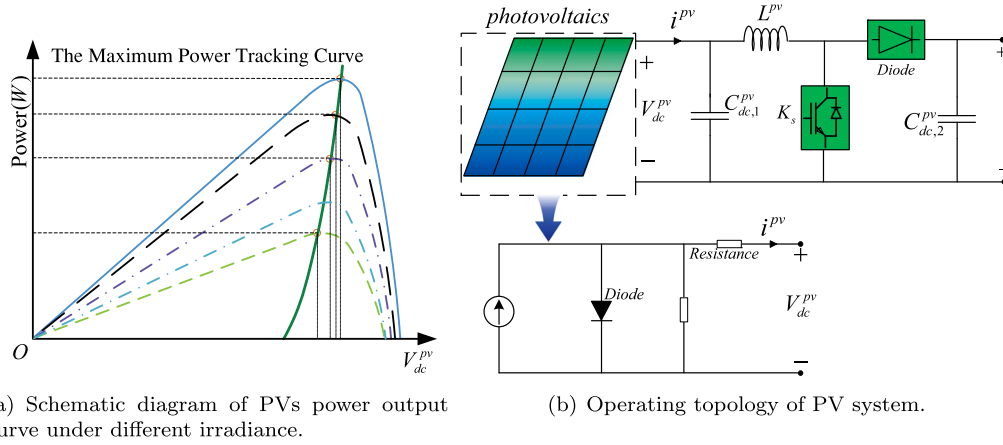
(b) Operating topology of PV system.

Fig. 2. The topology and power curve with PV system.

3. Designed SMC and Lyapunov stability for BESSs

In the configurations of BESSs delineated in [17], a battery is interfaced with a converter, the output of which is connected to a bus. Control of the converter's output power, and by extension, the battery's discharge or charge, is regulated through the assignment of a suitable duty cycle. Converters with the capacity for output power regulation via duty cycle modulation are thus considered integral to the proposed model. The DC-DC converter topologies that are relevant in this framework, illustrated in Fig. 3, are subject to further scrutiny. Employing the state-averaging method, according to Kirchhoff's law, the boost converter is analyzed [18]. The corresponding equation is formulated as follows:

Fig. 3. The topology of the Battery Energy Storage System.

$$\begin{cases} \dot{i}_i^b(t) = \dfrac{V_i^b}{L_i} - \dfrac{V_i^{dc}(t)}{L_i} + u_i(t)\dfrac{V_i^{dc}(t)}{L_i} \\ \dot{V}_i^{dc}(t) = -\dfrac{i_i^{bus}(t)}{C_i} + \dfrac{i_i^b(t)}{C_i} + u_i(t)\left(-\dfrac{i_i^b(t)}{C_i}\right) \end{cases}, \qquad (8)$$

where $i_i^b(t)$, $V_i^b(t)$, and $i_i^{bus}(t)$ represent the output current of the battery, the terminal voltage of the battery, and the output current of the converter in the ith BESS, respectively. The control signal $u_i(t)$, constrained within $[0, 1]$, is to be designed subsequently. The inductor and capacitor within the ith converter are denoted as L_i and C_i, respectively. It is assumed that switches K_1 and K_2 are ideal, not accounting for the voltage and current breakdown phenomena at high power.

Given the unpredictable nature of PV system output power in MPPT operation due to variable irradiance and temperature, the external
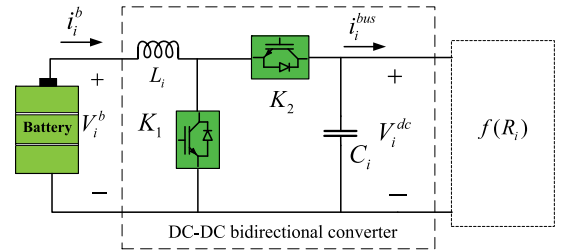
equivalent resistance for each BESS can be deduced. This resistance, denoted as R_i, is derived from the output voltage and current of the respective converters, shown in:

$$R_i = \frac{V_i^{dc}}{i_i^{bus}}, \qquad (9)$$

representing the equivalent resistance at the output of the ith BESS. The R_i is negative when the BESS is charging and positive during discharging, as indicated by the current and voltage reference directions in Fig. 3. There exists a boundary between the current of the bus, i_i^{bus}, and its voltage, V_i^{dc}, during the charging or discharging process. Due to fluctuations in PV energy, the external resistance, R_i, associated with each converter, is subject to variability. Thus, a nonlinear function is a

more accurate representation of R_i. Further, $f(R_i)$ can be expressed as:

$$f(R_i(t)) = \frac{V_i^{dc}(t)}{i_i^{bus}(t)}. \tag{10}$$

The above equation indicates that the equivalent resistance varies with time. Noted that $R_{i,1}$ and $R_{i,2}$ are the two boundaries for $f(R_i(t))$ in the ith BESS. The range of the equivalent resistance function, $f(R_i(t))$, is given as follows:

$$f(R_i(t)) \in \begin{cases} (-\infty, R_{i,1}], & \text{in charging state;} \\ [R_{i,2}, +\infty), & \text{in discharging state;} \\ \infty, & \text{otherwise.} \end{cases} \tag{11}$$

By equalizing the external resistances of the BESS units, each system can be analyzed independently, abstracting from the impedance and topological details of the microgrid.

In the discrete-time system, zero-order-holders are adopted for continuous variable $x(t)$, which means that $x(t) = x(kT_s)$ over time interval $[kT_s, (k+1)T_s]$ with T_s being the sampling period and $k \in \{0, 1, 2, \dots, \} = \mathcal{Z}$. For convenience of representation, abbreviate $x(kT_s)$ as $x(k)$.

Therefore, a mathematical model using Euler's discretization is applied to represent the DC-DC converter, which is given by:

$$\begin{cases} i_i^b(k+1) = i_i^b(k) + \frac{T_s V_i^b}{L_i} - \frac{T_s V_i^{dc}(k)}{L_i} + u_i(k)\frac{T_s V_i^{dc}(k)}{L_i} \\ V_i^{dc}(k+1) = V_i^{dc}(k) + \frac{T_s i_i^b(k)}{C_i} - \frac{T_s i_i^{bus}(k)}{C_i} - u_i(k)\frac{T_s i_i^b(k)}{C_i} \end{cases}. \tag{12}$$

Next, the SMC is designed based on the above discrete state equations.

This section presents the design of the SMC along with a comprehensive stability proof. In response to variable PV outputs, a discrete SMC is introduced to enhance tracking accuracy. Notably, Lemma 1 from [19] is fundamental to the core findings of this paper:

Lemma 1 (see [19]) : For the scalar dynamical system:

$$z(k+1) = z(k) + g(k) - \varepsilon \, sign(z(k)), \tag{13}$$

if $|g(k)| < \gamma$, $\gamma > 0$, and $\gamma < \varepsilon$, then the state z converges to the range confined by

$$|z| \le \varepsilon + \gamma < 2\varepsilon. \tag{14}$$

To accommodate variations in PV performance, a SMC with improved tracking performance is presented in this section. First, the sliding surface function design method is proposed to ensure that actual voltage, $V_i^{dc}(k)$, tracks reference voltage, $V_i^{dc,ref}(k)$, i.e. $V_i^{dc} = V_i^{dc,ref}$. The error variable, e_i, is defined as:

$$e_i(k) = V_i^{dc,ref}(k) - V_i^{dc}(k). \tag{15}$$

To better accommodate the fluctuations in PVs, the sliding surface function is designed as follows:

$$S_i(k) = \alpha_i e_i(k), \tag{16}$$

where α_i is a positive gain for the ith sliding surface function, the control signal $u_i(k)$ for switch K_1 in Fig. 3 is given by

$$u_i(k) = \frac{1}{2}[1 + sign(S_i(k))], \tag{17}$$

where $sign(\cdot)$ is the signal function.

Assumption 1. The three variables i_i^b, i_i^{bus} and V_i^{dc} of the ith converter in (8) are bounded and have upper bounds of $i_{i,max}^b$, $i_{i,max}^{bus}$, and $V_{i,max}^{dc}$, respectively.

Theorem 1. *For the DC-DC converter* (12) *and the SMC designed with* (15)–(17) *in the ith BESS, if Assumption 1 hold, there exists a finite number such that*

$$\lim_{k \to \infty} \left| V_i^{dc}(k) - V_i^{dc,ref}(k) \right| = \mathcal{O}(T_s), \tag{18}$$

which can guide its output voltage, $V_i^{dc}(k)$, to track the reference voltage, $V_i^{dc,ref}(k)$, for a limited time.

Proof. The SMC, designed with (15)–(17), uses the sliding mode surface function $S_i(k)$ in (16) to determine $S_i(k+1)$ at each step. In the discrete dynamical system model (12), $S_i(k+1)$ can be expressed as follows:

$$S_i(k+1) = \alpha_i e_i(k+1) = \alpha_i[V_i^{dc,ref}(k+1) - V_i^{dc}(k+1)]. \tag{19}$$

Based on (12), the sliding mode function at the $k+1$ step can be expressed as follows:

$$\begin{aligned} S_i(k+1) &= \alpha_i[v^{nom} - i_i^b(k+1)r_i - V_i^{dc}(k+1)] \\ &= \alpha_i[(v^{nom} - i_i^b(k)r_i - V_i^{dc}(k)) - u_i(k)(\frac{T_s r_i V_i^{dc}(k)}{L_i} - \frac{T_s i_i^b(k)}{C_i}) \\ &\quad - \frac{T_s r_i}{L_i}V_i^b + \frac{T_s r_i}{L_i}V_i^{dc}(k) - \frac{T_s i_i^b(k)}{C_i} + \frac{T_s i_i^{bus}(k)}{C_i}]. \end{aligned} \tag{20}$$

Based on (7) and (15), it is easy to demonstrate that $v^{nom} - i_i^b(k)r_i - V_i^{dc}(k) = e_i(k)$ in (20). By substituting (17) into (20), the term $S_i(k+1)$ can be reformulated as:

$$\begin{aligned} S_i(k+1) &= \alpha_i[e_i(k) - \frac{1}{2}(1 + sign(S_i(k)))(\frac{T_s r_i V_i^{dc}(k)}{L_i} - \frac{T_s i_i^b(k)}{C_i}) \\ &\quad - \frac{T_s r_i V_i^b}{L_i} + \frac{T_s r_i V_i^{dc}(k)}{L_i} - \frac{T_s i_i^b(k)}{C_i} + \frac{T_s i_i^{bus}(k)}{C_i}] \\ &= \alpha_i[e_i(k) - \frac{1}{2}(1 + sign(e_i(k)))T_s(\frac{r_i V_i^{dc}(k)}{L_i} - \frac{i_i^b(k)}{C_i}) \\ &\quad + T_s(\frac{r_i V_i^{dc}(k)}{L_i} - \frac{i_i^b(k)}{C_i}) + T_s(\frac{i_i^{bus}(k)}{C_i} - \frac{r_i V_i^b}{L_i})]. \end{aligned} \tag{21}$$

Let $\frac{r_i V_i^{dc}(k)}{L_i} - \frac{i_i^b(k)}{C_i} = \chi_i(k)$. $\chi_i(k)$ is bound by $|\chi_i(k)| = \left| \frac{r_i V_i^{dc}(k)}{L_i} - \frac{i_i^b(k)}{C_i} \right| \le \frac{r_i V_{i,max}^{dc}(k)}{L_i} + \frac{i_{i,max}^b(k)}{C_i} = \chi_{i,max}$. Consequently, (21) is rephrased to indicate that: (21) can be rewritten as:

$$\begin{aligned} S_i(k+1) &= \alpha_i e_i(k) - \frac{1}{2}\alpha_i T_s \chi_i(k) sign(S_i(k)) \\ &\quad + \alpha_i T_s(\frac{1}{2}\chi_i(k) + (\frac{i_i^{bus}(k)}{C_i} - \frac{r_i V_i^b}{L_i})) \\ &= S_i(k) - \frac{1}{2}\alpha_i T_s \chi_i(k) sign(S_i(k)) \\ &\quad + \alpha_i T_s(\frac{1}{2}\chi_i(k) + (\frac{i_i^{bus}(k)}{C_i} - \frac{r_i V_i^b}{L_i})) \end{aligned} \tag{22}$$

By invoking Lemma 1, it is implied that the criterion $\frac{i_i^{bus}(k)}{C_i} - \frac{r_i V_i^b}{L_i} < 0$ is inherently satisfied, a condition that is verified during the charging state of the ith BESS, where $i_i^{bus}(k) < 0$ when $f(R_i(k)) < 0$.

However, In the discharge state, it is necessary to ensure the boundedness of the sliding mode surface i.e. $\frac{i_i^{bus}(k)}{C_i} - \frac{r_i V_i^b}{L_i} < 0$. Therefore, the maximum tracking range of the voltage is given by:

$$V_i^{dc}(k) < \frac{r_i C_i V_i^b R_{i,2}}{L_i}. \tag{23}$$

Without considering physical constraints, (23) is the application range of the designed SMC.

In the context of the boundary of the sliding mode surface, it is acknowledged that the sampling time T_s is typically negligible, converging towards zero. Consequently, any quantity of the same order as T_s is represented using the notation $\mathcal{O}(T_s)$, which also approaches zero. Assume that (23) always holds, according to Assumption 2, the bound of (22) can be expressed as:

$$\begin{aligned} S_i(k+1) &= S_i(k) - \frac{1}{2}\alpha_i T_s \chi_i(k) sign(S_i(k)) \\ &\quad + \alpha_i T_s(\frac{1}{2}\chi_i(k) + (\frac{i_i^{bus}(k)}{C_i} - \frac{r_i V_i^b}{L_i})) \\ &\le S_i(k) - \frac{1}{2}\alpha_i T_s \chi_{i,max} sign(S_i(k)) \\ &\quad + \alpha_i T_s(\frac{1}{2}\chi_{i,max} + (\frac{i_i^{bus}(k)}{C_i} - \frac{r_i V_i^b}{L_i})), \end{aligned} \tag{24}$$

where the boundary is demarcated by:

$$|S_i(k)| \le \alpha_i T_s \chi_{i,max} = \mathcal{O}(T_s). \tag{25}$$

Given that T_s represents an infinitesimal quantity of the sampling time, it is deduced that the system trajectory can approach the vicinity of the sliding mode surface.

The previous analysis focused on the scenario where the BESS charge/discharge state remains constant over the sampling interval $t \in [kT_s, (k+1)T_s)$. However, for the sake of generalization, the situation where the equivalent resistance, $f(R_i(k))$, fluctuates within the same interval, is examined. It is assumed that $f(R_i(k))$ undergoes a sign change at some point within $t \in [kT_s, (k+1)T_s)$. The sequence of moments within this interval is defined as $t \in [kT_s, (k+1)T_s)$ be: $t_k = kT_s < t_{k_0} < t_{k_1} < \cdots < t_{k_{s-1}} < t_{k_s} < \cdots < t_{k_l} < t_{k+1} = (k+1)T_s$. It is also assumed that $f(R_i(k))$ remains unchanged within any subset $t \in [kT_s, (k+1)T_s)$, and therefore (25) is valid for any arbitrary $0 \leq t_s \leq t_l$. This analysis shows that even when $f(R_i(k))$ experiences a sign shift during the sampling period $t \in [kT_s, (k+1)T_s)$, Theorem 1 is still applicable. It is worth noting that the above is dependent on the converter's topology. Once the SMC is designed and the proof process may not be applied when the topology is changed.

Remark 1. It is observed that the proposed SMC exhibits enhanced resilience to PV disturbances compared to conventional linear controllers, attributable to the incorporation of a nonlinear BESS model. When (16) and (17) are considered in conjunction, the influence of the SMC's parameters on controller stability appears marginal. Stability is primarily ensured by the positivity of the sliding mode surface. This positivity, in turn, affects the conduction states of switches K_1 and K_2 in the converter, regardless of the sliding mode surface characteristics.

4. Voltage regulation

The SoC balancing strategy, which is a power distribution method, faces the challenge of balancing voltage regulation with SoC equilibrium due to differences in line impedance and battery capacity [20]. To address this issue, distributed voltage estimation is used to determine the average bus voltage, and voltage regulation is employed to correct the voltage deviation caused by droop control.

Firstly, a compromise method is adopted to regulate the weighted average voltage of all BESSs to an acceptable range. To this end, a method of distributed voltage estimation instead of actual voltage is adopt here [21]. The estimate voltage is

$$\hat{V}_i^{dc}(k) = V_i^{dc}(k) + \varsigma_i \sum_{n=0}^{k} T_s \sum_{j \in N_i} a_{ij}(\hat{V}_j^{dc}(n) - \hat{V}_i^{dc}(n)), \quad (26)$$

where $\hat{V}_{dc,i}$ denoted the estimate value of measured voltage $V_{dc,i}(k)$, ς_i is a positive value in ith BESS. Based on (26), any voltage deviations can be directly estimated in distributed with the adjacency network N_i. Thus, the voltage consensus can be obtained as $\lim_{k \to \infty}(\hat{V}_{dc,i}(k) - \frac{1}{M} \sum_{j=1}^{M} V_{dc,j}(k)) = 0$, where M is the numbers of BESSs.

Droop control inherently introduces a voltage offset, potentially degrading bus voltage quality and compromising load operation. To mitigate this, a voltage restoration technique is introduced to enhance the reliability of the power supply for all BESS units. The nominal voltage, v_i^{nom}, within the established droop control framework (7), must be adjusted to counteract the voltage offset. Accordingly, a voltage regulation strategy informed by a consensus algorithm [21] is applied:

$$v_i^{nom}(k) = \sum_{n=0}^{k} T_s[\eta_i(v^{nom} - \hat{V}_i^{dc}(n)) + \sum_{j \in N_i} a_{ij}\omega_i(\hat{V}_j^{dc}(n) - \hat{V}_i^{dc}(n))], \quad (27)$$

where v_i^{nom} represents the voltage regulation value for ith BESS and v^{nom} is the set point with η_i and ω_i are the two positive gain. Hence, the droop control strategy (7) based on voltage regulation can be rewritten as:

$$V_i^{dc,ref}(k) = v_i^{nom}(k) - i_i^b(k)r_i. \quad (28)$$

Accordingly, v_i^{nom} is adjusted to negate the voltage offset induced by droop control. The subsequent section proposes a SoC balancing control strategy utilizing sliding mode control, enhancing the allocation of output power across BESS units through the adjustment of the droop factor r_i.
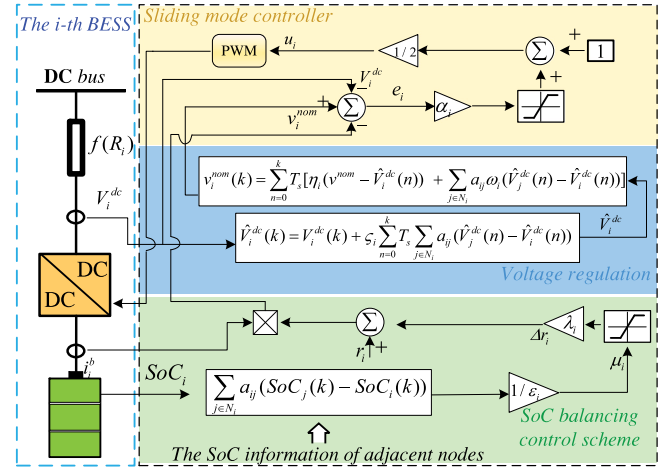

Fig. 4. The flowchart for the ith BESS.

5. SoC balancing control strategy

5.1. Modeling of BESSs

In PV-based microgrids, BESSs serve as a buffering interface between photovoltaic sources and loads, which is crucial for microgrid stability. Consequently, the goal of SoC balancing is to enhance the longevity of the BESSs. The SoC indicates the remaining battery capacity. Within BESSs, the SoC for each battery unit is defined as follows [22]:

$$SoC_i(t) = SoC_i(t_0) - \frac{\int_{t_0}^{t} i_i^b(t)dt}{Q_i}, \quad (29)$$

for all $i = 1, 2, \ldots, M$, where SoC_i, Q_i and i_i^b denoted the SoC, capacity and output of the current in the ith BESS, respectively. However, in a discrete system, this expression is reformulated as [23]

$$SoC_i(k+1) = SoC_i(k) - \frac{T_s i_i^b(k)}{Q_i}. \quad (30)$$

5.2. A novel distributed SoC balancing method

To achieve a balance in SoC, the droop offset coefficient $\tilde{r}_i$ is used to modulate the reference voltage $V_i^{dc,ref}$ as specified in (28). Moreover, in a PV-based microgrid, the bidirectional flow of current during BESS charge and discharge cycles requires the consideration of current direction. The direction of current flow from the battery to the microgrid is considered positive. Considering the two situations of charging and discharging, it is necessary to adjust (28) to eliminate the influence of the change of i_i^b on the droop control (see Fig. 4). Consequently, Eq. (28) can be further rewritten as:

$$V_i^{dc,ref} = v_i^{nom} - i_i^b(k)(r_i + sign(i_i^b(k))\tilde{r}_i(k)). \quad (31)$$

To facilitate SoC balancing among BESS units, the variable μ_i is introduced as follows:
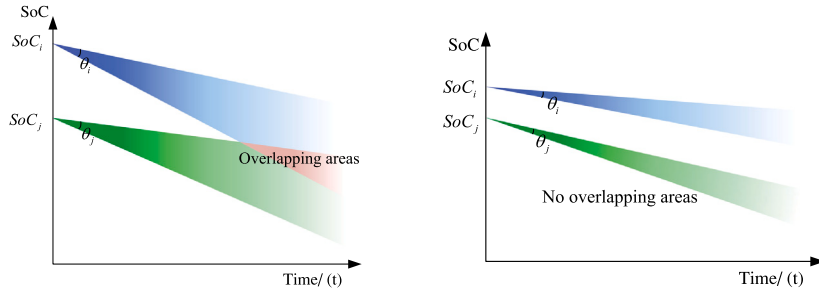
$$\mu_i(k) = \sum_{j \in N_i} a_{ij}(SoC_j(k) - SoC_i(k)), \quad (32)$$

where N_i represents the set of nodes neighboring the ith BESS unit. The offset coefficient $\tilde{r}_i$ is designed as:

$$\Delta r_i(k) = \lambda_i sat(\frac{\mu_i(k)}{\varepsilon}), \quad (33)$$

where λ_i and ε being positive, and $sat(x)$ denotes a saturation function, which can be written as:

$$sat(x) = \begin{cases} x & \text{if } |x| \leq 1 \\ sign(x) & \text{if } |x| > 1 \end{cases}. \quad (34)$$

(a) The rate change of SoC for the two adjacent nodes when Assumption 2 hold.

(b) The rate change of SoC for the two adjacent nodes when Assumption 2 dose not hold.

Fig. 5. Regulation interval of SoC_i by λ_i.

Existing literature, such as [20], has explored the nonlinear dynamics between the battery current i_i^b and the control signal u_i. Building on these analyses, the subsequent section will detail the derivation of the specific relationship between i_i^b and the DC voltage V_i^{dc}.

Neglecting the converter's internal resistance losses allows the assumption that the output power is conserved across the converter [24, 25], i.e.

$$i_i^b(k)V_i^b = V_i^{dc}(k)i_i^{bus}(k). \tag{35}$$

Let $i_i^{bus}(k) = V_i^{dc}(k)/f(R_i(k))$, (35) can be rewritten as:

$$i_i^b(k) = \frac{[V_i^{dc}(k)]^2}{V_i^b f(R_i(k))} = \frac{V_i^{dc}(k)}{V_i^b |f(R_i(k))|} sign\left(\frac{1}{f(R_i(k))}\right)V_i^{dc}(k). \tag{36}$$

Eq. (36) indicates that the sign of $f(R_i(k))$ determines the charge/discharge state in the ith BESS. Therefore, a reasonable equivalence of $f(R_i(k))$ can be obtained the following relationship between $i_i^b(t)$ and $V_i^{dc}(t)$, i.e.

$$i_i^b(k) = \beta_i(k)(V_i^{dc}(k) - \gamma_i(k)), \tag{37}$$

where $\beta_i(k) = \frac{V_i^{dc}(k)}{V_i^b |f(R_i(k))|}$ is a bounded nonlinear function for the ith BESS, in which $\beta_{i,max}$ and $\beta_{i,min}$ are the upper bounded and lower bounded, respectively. $\gamma_i(k)$ is a variable factor that controls the charge/discharge state of the ith BESS.

In general, the value of $\gamma_i(k)$ is determined by the power difference between PVs and loads in the microgrid, which is given by:

$$\gamma_i(k) = \begin{cases} 0 & \text{charging;} \\ 2V_i^{dc}(k) & \text{discharging.} \end{cases} \tag{38}$$

In a conventional PV-based microgrid, the BESS's charging/discharging states and the equivalent external resistance are impacted by PV output power. Hence, $\beta_i(k)$ and $\gamma_i(k)$ are represented as nonlinear functions to express the unregulated effects of PV outputs. As inferred from (35), adjusting V_i^{dc} facilitates indirect control over i_i^b output. Given that V_i^{dc} sets the converter's output power, which subsequently affects the BESS's output, $\beta_i(k)$ is considered positive in (37).

5.3. System stability for SoC balancing

To prepare for the analysis of system stability, the following symbolic definitions are established. For arbitrary column vector $X_1 = [x_{1,1}, x_{1,2}, \ldots, x_{1,M}]^T$ or diagonal matrix $X_2 = diag(x_{2,1}, x_{2,2}, \ldots, x_{2,M})$, the symbol $|\cdot|$ represents the element-wise absolute value, resulting in $|X_1| = [|x_{1,1}|, |x_{1,2}|, \ldots, |x_{1,M}|]^T$ and $|X_2| = diag(|x_{2,1}|, |x_{2,2}|, \ldots, |x_{2,M}|)$, respectively. With this in place, the global stability of the proposed SoC balancing control approach for a microgrid system with M BESS units will be assessed. Denoting $SoC(k) = [SoC_1(k), SoC_2(k), \ldots, SoC_M(k)]^T$ as the collective SoC values, (30) is reformulated as:

$$SoC(k+1) = SoC(k) - T_s Q^{-1} I^b(k), \tag{39}$$

where $Q = diag(Q_1, Q_2, \ldots, Q_M)$ and $I^b(k) = [i_1^b(k), i_2^b(k), \ldots, i_M^b(k)]^T$ denote the set of Q_i and i_i^b, respectively.

Then, the set of output voltage $V_i^{dc,ref}$ is defined as $V^{dc,ref}(k) = [V_1^{dc,ref}(k), V_2^{dc,ref}(k), \ldots, V_M^{dc,ref}(k)]^T$. Based on (31), $V^{dc,ref}$ can be expressed as below:

$$V^{dc,ref}(k) = V^{nom} - \Lambda I^b(k) - \tilde{\Lambda}(k) \odot sig(I^b(k)) \odot I^b(k), \tag{40}$$

where $\odot$ represents the Hadamard product. Let $V^{nom} = [v_1^{nom}, v_2^{nom}, \ldots, v_M^{nom}]^T$, $\Lambda = diag(r_1, r_2, \ldots, r_M)$ and $\tilde{\Lambda} = [\tilde{r}_1(k), \tilde{r}_2(k), \ldots, \tilde{r}_M(k)]^T$ be the set of v_i^{nom}, r_i and $\tilde{r}_i(k)$, respectively. Base on (33), $\tilde{\Lambda}(k)$ is given as

$$\tilde{\Lambda}(k) = \Xi Sat\left(\frac{-L(\mathcal{G})SoC(k)}{\varepsilon}\right), \tag{41}$$

where $\Xi = diag(\lambda_1, \lambda_2, \ldots, \lambda_M)$ is the set of λ_i, and for an arbitrary column vector $X = [x_1, x_2, \ldots, x_M]^T$, $Sat(X) = [sat(x_1), sat(x_2), \ldots, sat(x_M)]^T$ is the set of saturation function. Then, the set of i_b^i can be expressed as

$$I^b(k) = \Gamma(k)[V^{dc}(k) - Y(k)], \tag{42}$$

where $\Gamma(k) = diag(\beta_1(k), \beta_2(k), \ldots, \beta_M(k))$ and $Y(k) = [\gamma_1(k), \gamma_2(k), \ldots, \gamma_M(k)]^T$ denoted the set of $\beta_i(k)$ and $\gamma_i(k)$, respectively.

It is worth noting that the stability of the controller has been proved before, assume $V_i^{dc,ref} = V_i^{dc}$. From (40) and (42), the relationship between $I^b(k)$ and $\tilde{\Lambda}(k)$ can be observed as:

$$\begin{aligned} I^b(k) = &(I_M + \Lambda\Gamma(k))^{-1}\Gamma(k)V^{nom} \\ &- (I_M + \Lambda\Gamma(k))^{-1}\Gamma(k)\tilde{\Lambda}(k)|I^b(k)| \\ &- (I_M + \Lambda\Gamma(k))^{-1}\Gamma(k)Y(k), \end{aligned} \tag{43}$$

where $I_M \in R^{M \times M}$ is the identity matrix, the set of SoC can be rewritten as:

$$\begin{aligned} SoC(k+1) = &SoC(k) - T_s(Q + Q\Lambda\Gamma(k))^{-1}\Gamma(k)V^{nom} \\ &+ T_s(Q + Q\Lambda\Gamma(k))^{-1}\Gamma(k)\tilde{\Lambda}(k) \odot |I^b(k)| \\ &+ T_s(Q + Q\Lambda\Gamma(k))^{-1}\Gamma(k)Y(k). \end{aligned} \tag{44}$$

Further, let $A(k) = diag(a_1(k), a_2(k), \ldots a_M(k))$ with $A(k) = (Q + Q\Lambda\Gamma(k))^{-1}\Gamma(k)$, (44) can be rewritten as:

$$SoC(k+1) = SoC(k) + T_s A(k)\tilde{\Lambda}(k) \odot |I^b(k)| - T_s A(k)[V^{nom} - Y(k)]. \tag{45}$$

For simplicity, Let $a_i^*(k)$ denotes $a_i(k)[v_i^{nom} - \gamma_i(k)]$, the set of $a_i^*(k)$ can be expressed as $A^*(k) = diag(a_1^*(k), a_2^*(k), \ldots, a_M^*(k))$. Similarly $B^*(k) = diag(b_1^*(k), b_2^*(k), \ldots, b_M^*(k))$ is the set of $b_i^*(k)$ within $b_i^*(k) = a_i(k)|i_i^b(k)|\lambda_i$. Moreover, (45) can be rewritten as:

$$SoC(k+1) = SoC(k) - T_s A^*(k)\mathbf{1}_M + T_s B^*(k)\mathbf{1}_M \odot Sat\left(-\frac{L(\mathcal{G})SoC(k)}{\varepsilon}\right). \tag{46}$$

Next, the following assumption based on [26] is giving.

Assumption 2. For any two BESS nodes (marked the ith BESS and the jth BESS), assume $\rho(k)$ is a known function and $a_i^*(k)$ and $a_j^*(k)$ satisfy the inequality $a_i^*(k) - a_j^*(k) \leq \rho_{ij}(t)$. Then, Ξ can be determined separately under which values of λ_i and λ_j can satisfied, possibly in steady state, as follows

$$b_i^*(k) + b_j^*(k) \geq \rho_{ij}(k) + \rho_0, \tag{47}$$

where $\rho_0 > 0$ is some given constant.

Remark 2. It is important to note that Assumption 2 is necessary to ensure the stability of the Lyapunov function in the analysis below which is the application range for the proposed SoC balancing control strategy. It may not always hold true in a PV-based microgrid, due to some practical limitations. For instance, the SoC equilibrium of the BESS cannot be achieved when the BESS output power is zero ($P_{BESS_i} = 0$) [20]. Moreover, there may be transitory deviations from Assumption 2 during charging and discharging due to the inductive nature of the grid lines and current continuity. While these deviations are brief and can be observed in simulation studies, the parameter λ_i can be adjusted to regulate $\tilde{r}_i(k)$ and ensure that the adherence to Assumption 2 is as close as possible (see Fig. 5).

Theorem 2. Assume Assumption 2 holds, the SoCs can eventually be achieved consistently, i.e,

$$\lim_{k \to \infty} \left| SoC_i(k) - SoC_j(k) \right| = 0, \forall (i, j) \in \mathcal{V}. \tag{48}$$

Proof. The proof is divided into three steps.

Step(I) (Constructing Lyapunov functions and linear decompositions of graph): To verify the stability of the proposed control strategy, a Lyapunov function is constructed to represent the difference between different BESSs. Considering the entire microgrid system with M nodes. Define $Y(k) = B^T(G)SoC(k)$, here the Lyapunov function is given by

$$\begin{aligned} E(Y(k)) &= Y^T(k)Y(k) \\ &= SoC^T(k)B(G)B^T(G)SoC(k) \\ &= SoC(k)L(\mathcal{G})SoC(k) \geq 0. \end{aligned} \tag{49}$$

Note that (49) can be rewritten as $E(Y(k)) = \sum_{i=1, j \in N_i}^{M} \left(SoC_i(k) - SoC_j(k) \right)^2 \geq 0$. According to the Lyapunov stability theory, $\Delta E(Y(k))$ must be negatively to ensure the system stability under the SoC cooperative control strategy, i.e., the SoC of each BESS remains consistent.

Let $\Delta SoC(k) = SoC(k+1) - SoC(k)$ be the increment of the Lyapunov function, which can be expressed as:

$$\begin{aligned} \Delta E(Y(k)) &= SoC^T(k+1)L(\mathcal{G})SoC(k+1) - SoC^T(k)L(\mathcal{G})SoC(k) \\ &= [\Delta SoC(k) + SoC(k)]^T L(\mathcal{G})[\Delta SoC(k) + SoC(k)] \\ &\quad - SoC^T(k)L(\mathcal{G})SoC(k) \\ &= \Delta SoC^T(k)L(\mathcal{G})\Delta SoC(k) \\ &\quad + \Delta SoC^T(k)L(\mathcal{G})SoC(k) + SoC^T(k)L(\mathcal{G})\Delta SoC(k) \end{aligned} \tag{50}$$

In fact, $\Delta SoC^T(k)L(\mathcal{G})\Delta SoC(k)$ can be viewed as a higher order infinitesimal term. Hence, (50) can be rewritten as:

$$\Delta E(Y(k)) = 2\Delta SoC^T(k)L(\mathcal{G})SoC(k). \tag{51}$$

Following this line, (51) can be rewritten as follows combined with (45),

$$\Delta E(Y(k)) = 2T_s[-A^*(k)1_M + B^*(k)1_M \odot Sat\left(\frac{-L(\mathcal{G})SoC(k)}{\varepsilon}\right)]^T$$
$$\times L(\mathcal{G})SoC(k). \tag{52}$$

Note that $L(\mathcal{G})SoC(k) = [\delta_1, \delta_2, \ldots, \delta_M]^T$, while $\delta_{\min}$ is the minimum value in the column vector. The case of $\delta_{\min} > 1$ is considered. Combine

with (41) and (52), we can get that

$$\begin{aligned} \Delta E(Y(k)) &= -2T_s 1_M^T A^*(k)L(\mathcal{G})SoC(k) \\ &\quad + [2T_s 1_M^T B^*(k) \odot sig^T(-L(\mathcal{G})SoC(k))L(\mathcal{G})SoC(k)] \\ &= -2T_s 1_M^T A^*(k)L(\mathcal{G})SoC(k) - 2T_s 1_M^T B^*(k)|L(\mathcal{G})SoC(k)|. \end{aligned} \tag{53}$$

Step(II) (Linear decompositions of graph [27]): Considering that $\mathcal{G}$ has N edges, the graph can be decomposed into a sum of several subgraphs, Let $\mathcal{G}_i$ is the subgraphs of $\mathcal{G}$ that only has one edge. Then, it is easy to get that

$$\begin{cases} \mathcal{G}_1 \cap \mathcal{G}_2 \cap \mathcal{G}_3 \cdots \cap \mathcal{G}_N = \emptyset \\ \mathcal{G}_1 \cup \mathcal{G}_2 \cup \mathcal{G}_3 \cdots \cup \mathcal{G}_N = \mathcal{G} \end{cases}, \tag{54}$$

$$L(\mathcal{G}) = \sum_{i=1}^{N} L(\mathcal{G}_i). \tag{55}$$

Therefore, for arbitrary two nodes i and j in $\mathcal{G}_i$, assume $SoC_i > SoC_j$ and $(i, j) \subset \mathcal{E}_i$, (53) can be rewritten as

$$\begin{aligned} \Delta E(Y(k)) &= -\sum_{i=1}^{N}[2T_s 1_M^T A^*(k)L(\mathcal{G}_i)SoC(k) + 2T_s 1_M^T B^*(k)|L(\mathcal{G}_i)SoC(k)|] \\ &= -2T_s \sum_{i=1}^{N}[(a_i^*(k) - a_j^*(k))(SoC_i(k) - SoC_j(k)) \\ &\quad + (b_i^*(k) + b_j^*(k))(SoC_i(k) - SoC_j(k))]. \end{aligned} \tag{56}$$

Step(III) (Proof that $\Delta E(Y(k)) < 0$ based on Assumption 2 and the Lyapunov stability on SoC balancing control strategy): For any subgraph $\mathcal{G}_i$, there is the following relationship based on Assumption 2

$$\begin{aligned} &[(a_i^*(k) - a_j^*(k))(SoC_i(k) - SoC_j(k)) + (b_i^*(k) + b_j^*(k))(SoC_i(k) - SoC_j(k))] \\ &\geq [\rho_{ij}(k) + (b_i^*(k) + b_j^*(k))](SoC_i(k) - SoC_j(k)) \\ &> [\rho_{ij}(k) + \rho_0(k) + (b_i^*(k) + b_j^*(k))](SoC_i(k) - SoC_j(k)) > 0. \end{aligned} \tag{57}$$

Based on above analysis, the following can be found:

$$\Delta E(Y(k)) < 0. \tag{58}$$

According to (49) and (58), the Lyapunov function is stability when there is an inequality of SoC between the energy storage nodes,

$$\begin{cases} E(Y(k)) > 0 \\ \Delta E(Y(k)) < 0 \end{cases}, \tag{59}$$

which indicates that all SoCs can be guide the same value, i.e. $SoC_1(k) = SoC_2(k) = \cdots = SoC_M(k)$ for $k \to \infty$.

6. Case studies

In order to test the effectiveness of the suggested distributed SoC balancing control strategy and the performance of the designed SMC when single-diode PV systems are perturbed, we have set up a network consisting of five BESSs and a PV system with four loads. In this section, we present some case studies to confirm the efficiency of the proposed controller and the innovative SoC balancing control strategy.

The network topology, consisting of five BESS nodes with communication links, is illustrated in Fig. 6. The parameters are listed in Table 1. The effectiveness of the SoC balancing control strategy under load fluctuations and communication packet loss is initially verified through simulation. Later, the strategy's efficiency is confirmed in the presence of PV influences. Finally, the robustness of the SMC is demonstrated through comparative analysis with established controllers. It is important to note that the BESS control strategy is evaluated using the PV system as a disturbance factor. The simulations are conducted with

Table 1
Simulation parameters of SoC balancing.

Type	Electrical parameter
Sampling time	1×10^{-3} s
Capacitance of converters	$C_i \in \{0.25, 0.25, 0.2, 0.1, 0.2\}$ F
Inductance of converters	$L_i \in \{102, 100, 120, 100, 103\}$ mH
Nominal voltage of battery	$V^b = 285$ V
Set point voltage	$v^{nom} = 380$ V
Capacity of battery	$Q_i \in \{10, 10.1, 10.2, 10.3, 10.4\}$ Ah
Initial SoC	$SoC_i(0) \in \{70, 68, 66, 64, 62\}\%$
Line impedance	$R_{1,2} = (0.1\Omega + 0.01$ H$)$, $R_{2,3} = (0.2\Omega + 0.015$ H$)$
	$R_{3,4} = (0.15\Omega + 0.01$ H$)$, $R_{4,5} = (0.2\ \Omega + 0.05$ H$)$
	$R_{1,pv} = R_{5,pv} = (0.1\ \Omega + 0.005$ H$)$
	$R_i \in \{0.05, 0.05, 0.04, 0.05, 0.04\}\ \Omega$
Parallel strings of PVs	25
Series-connected modules per string of PVs	35
Standard Test Conditions (STC)	irradiance = 1000 W/m^2, temperature = 25°C
Maximum Power	213.15 W
Open circuit voltage	36.3 V
Short-circuit current	7.84 A
Load$_1$	10 kW
Load$_2$	5 kW
Load$_3$	3 kW
Load$_4$	10 kW

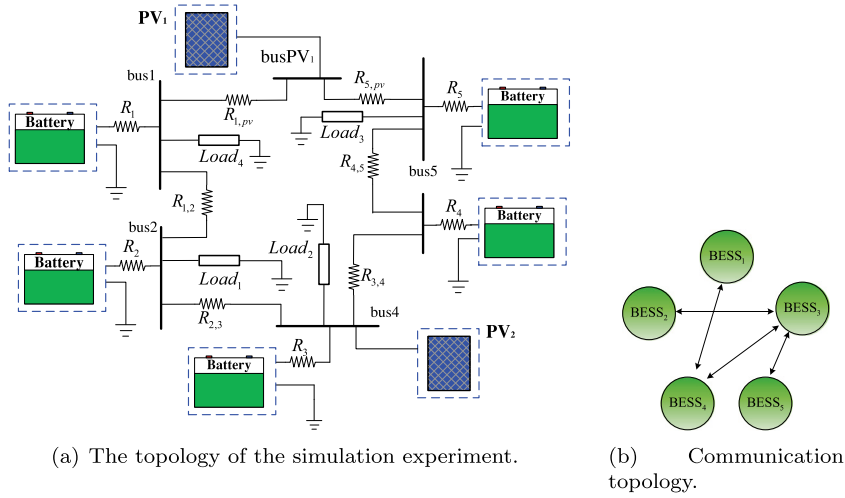(a) The topology of the simulation experiment.   (b)   Communication topology.

Fig. 6. The physical topology of the simulation experiment.

the PV system operating in MPPT mode and providing variable output power [28].

6.1. The robustness for SoC balancing control strategy

The simulation considers a scenario where sudden load changes test the effectiveness of the proposed SoC balancing control strategy. Initially, Load$_1$, Load$_2$, and Load$_4$ are connected to the microgrid, with the five BESS units providing power. The BESS units are expected to be discharging at this stage. Furthermore, Load$_3$ connects at $t = 150$ s and Load$_4$ disconnects at $t = 250$ s.

Fig. 7 illustrates the SoC control strategy's resilience under plug-and-play conditions, showing that changes in load do not compromise SoC consistency. Additionally, increased loads result in a rapid decrease in SoC, due to the higher output required from each BESS to sustain the loads.

Moreover, the output voltage V_i^{dc} and estimated voltage $\hat{V}_i^{dc}$ of the BESS units are observable in Fig. 8(a) and 8(b), respectively. Voltage regulation and the SoC balancing control strategy maintain V_i^{dc} around 380 V to ensure load operation, with the operation voltage autonomously adjusted based on SoC, as seen in Fig. 8(a). Meanwhile, the estimated voltage converges towards 380 V, noted in Fig. 8(b). Combining observations from Figs. 7 and 8, it is evident that the SoC
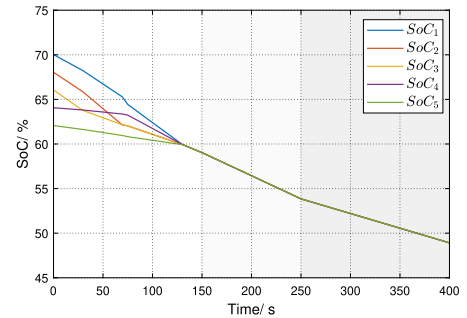

Fig. 7. The evolution of SoCs.

balancing strategy achieves equilibrium among SoCs. Additionally, the implemented observer and voltage management strategy effectively mitigate voltage deviations resulting from droop control.

Figs. 9(a) and 9(b) illustrate the power allocation mechanism inherent in the SoC balancing control strategy. Power in each BESS reacts to changes in the reference deviation $\Delta \tilde{r}_i$, guided by (31) (33). Fig. 9(a) depicts the adjustment of $\Delta \tilde{r}_i$ in relation to SoC shifts within each BESS, as directed by the control strategy. Fig. 9(b) confirms that the
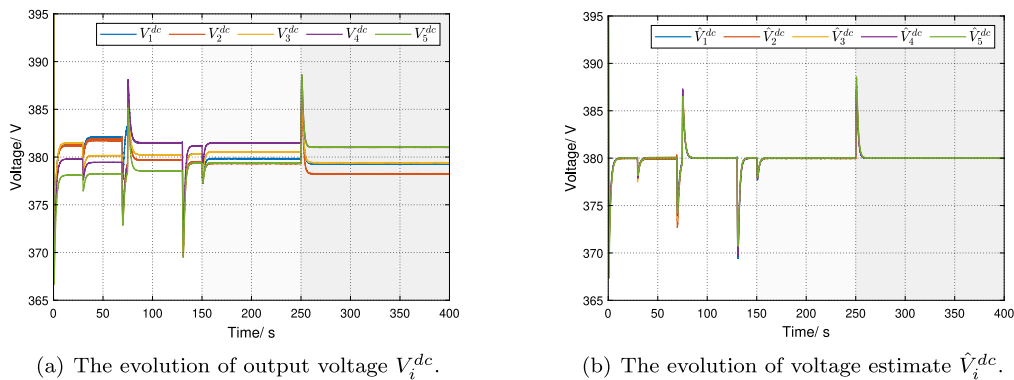
(a) The evolution of output voltage V_i^{dc}.

(b) The evolution of voltage estimate $\hat{V}_i^{dc}$.

Fig. 8. The simulation results of V_i^{dc} and $\hat{V}_i^{dc}$, respectively.

(a) The evolution of Δr_i.

(b) The evolution of output power P_{BESS_i}.
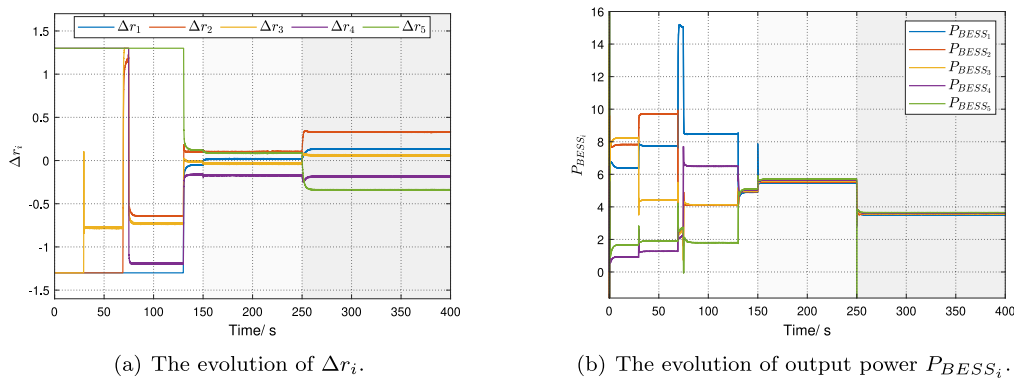
Fig. 9. The simulation results for SoC balancing factor Δr_i and output power P_{BESS_i}.

(a) The evolution of SoCs based on 50% packet loss.

(b) The evolution of V_1^{dc} based on packet loss.
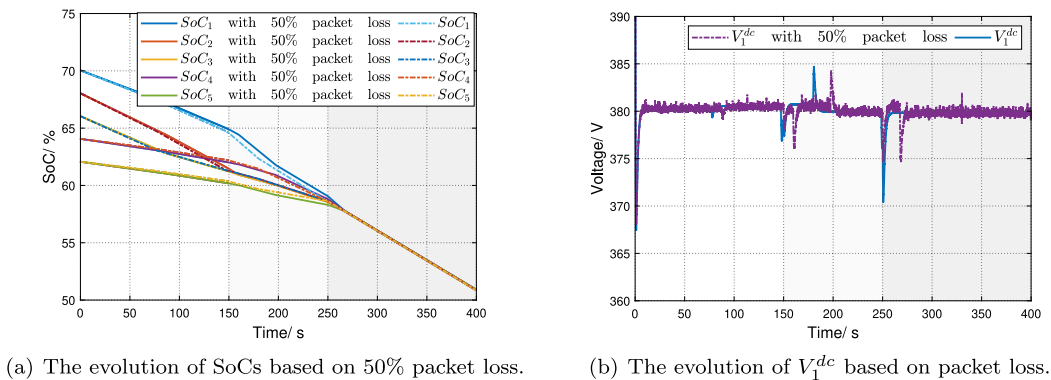
Fig. 10. The effect of packet loss on simulation results.
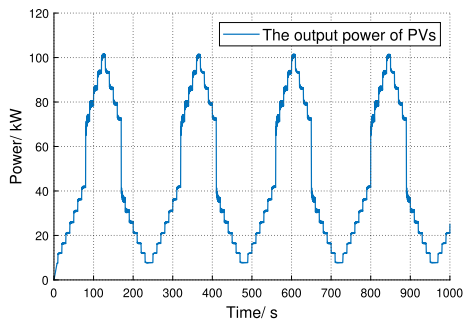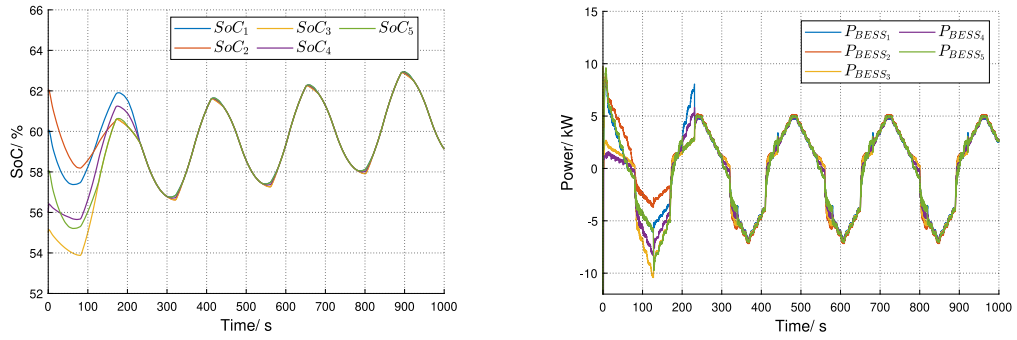

Fig. 11. The output power of PVs.

fluctuations in $\Delta \tilde{r}_i$ are consistent with the output power fluctuations of the BESSs. SoC equilibrium is achieved among the BESS units after roughly 175 s, with power output per BESS unit stabilizing near 3.6 kW. The disconnection of Load4 at 250 s results in a change in power output to about 4.8 kW, with the 10 kW reduction being evenly shared by the BESS units.

The presented SoC balancing control strategy has proven to be highly resilient to packet loss, as demonstrated in Fig. 10. Packet loss typically affects the cooperative efficiency of SoC management, but the discrepancy between the solid line (representing a scenario with 50% packet loss) and the dashed line (representing no packet loss) is minimal. This suggests that the impact of packet loss can be considered negligible, as shown in Fig. 10(a). It is worth noting that packet loss induces voltage chatter in BESS$_1$'s output voltage.

(a) The SoCs evolution of five BESSs under the influence of PVs.

(b) The evolution of the output power P_{BESS_i}.

Fig. 12. Simulation results under PVs operation.

(a) The communication topology.
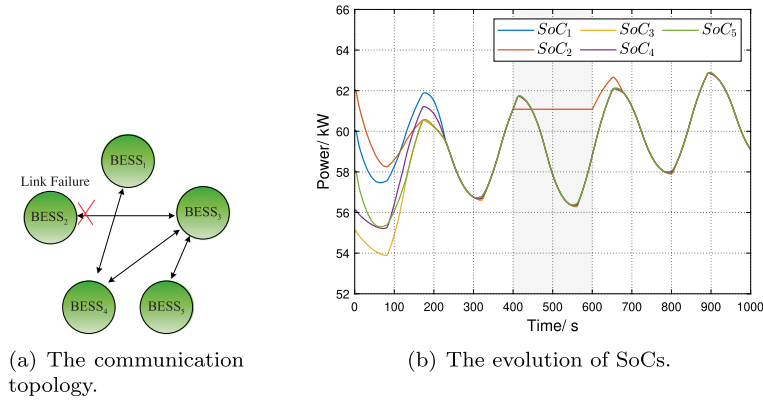

(b) The evolution of SoCs.

Fig. 13. The simulation result in the 2nd BESS failure state.

6.2. Nonlinear SoC balancing control strategy

The SoC balancing control strategy and SMC approach under study demonstrate considerable robustness to PV-induced fluctuations. Fig. 11 displays the PV output power, focusing on a scenario initiated solely with PV_1 to simplify the analysis of the interaction between PV output and BESS performance. Initial SoC values are designated as 60% for SoC_1, 62% for SoC_2, 55% for SoC_3, 56% for SoC_4, and 58% for SoC_5. In this scenario, all loads are connected at the onset ($t = 0$ s), and the simulation timeframe is established at 1000 s.

The evolution of the SoC during PV operations is detailed in Fig. 12(a). The five BESSs are engaged in a continuous cycle of charging and discharging to counteract the fluctuating power outputs from the PVs. At approximately 160 s into the operation, the five BESS units achieve a state of SoC balance as a result of the implemented SoC balancing control strategy. However, there is a brief period of imbalance observed when the systems transition between charging and discharging modes, attributable to the inductive impedances present within the microgrid. Despite this, the SoC balance is reestablished shortly after these transient imbalances occur.

Fig. 12(b) illustrates the dynamics of the output power for the five BESS units, highlighting the switch between charging and discharging states. This behavior is governed by the SoC balancing control strategy. After achieving SoC balance at around 160 s, the output power of the BESS units continues to converge, suggesting a stable operational state has been reached. When considering the information in both Fig. 11 and Fig. 12(b), it becomes evident that the power output of the BESSs effectively counterbalances the output power of the PVs. This demonstrates that the BESSs serve as a buffer, absorbing or releasing
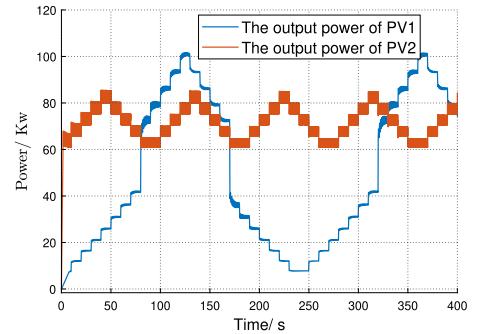

Fig. 14. The output power of PVs.

power as needed to compensate for the variability of the PV output, thus ensuring the maintenance of SoC balance across all nodes as dictated by the control strategy. Following this analysis, the issue of link failures within the system is addressed next.

In the simulation, conditions are kept constant as $BESS_2$ is disconnected at 400 s and reconnected at 600 s. The communication topology for this simulation is presented in Fig. 13(a), with the corresponding results displayed in Fig. 13(b). During the interval $[400, 600]$ s, SoC_2 remains unchanged due to the disconnection of $BESS_2$, while the other BESS units maintain the SoC balance. Upon reconnection at 600 s, $BESS_2$ realigns its output to restore SoC balance, enabling all five BESS units to achieve equilibrium in accordance with the SoC balancing strategy.
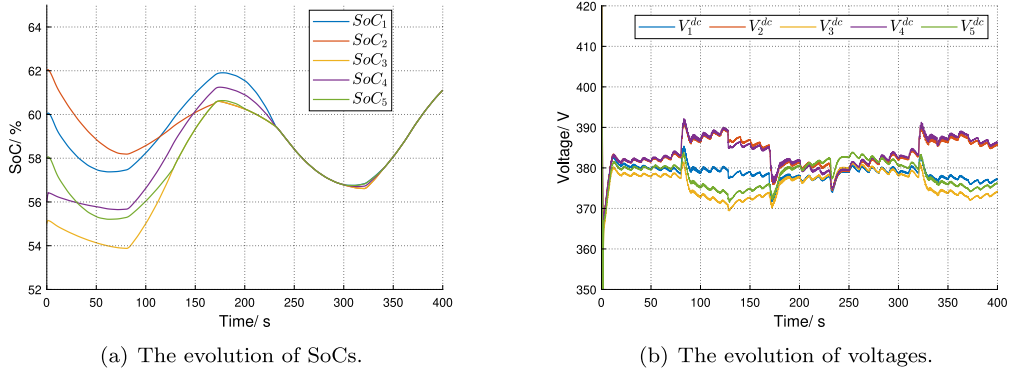
(a) The evolution of SoCs.

(b) The evolution of voltages.

Fig. 15. The evolution of SoC and voltage for BESSs under PVs perturbation.
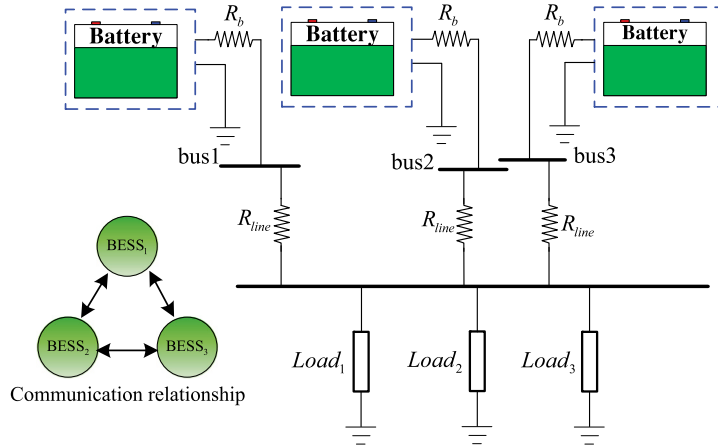

Fig. 16. The physical topology of the compared case.

Subsequently, PV_1 and PV_2 are activated simultaneously to assess the control strategy's effectiveness with multiple PV and BESS inputs. The variability of PV_2 output is increased to ensure the strategy's validity over a wider range of conditions, as illustrated in Fig. 14.

Figs. 15(a) and 15(b) demonstrate the SoC and voltage of five BESSs operating under multiple PV panels. As depicted in Fig. 15(a), the SoCs of all five BESSs are consistently maintained at similar levels through the proposed SoC cooperative control strategy. Despite fluctuations in the PV output power, voltage regulation controls the BESS output voltage, which remains close to the 380 V set value, as shown in Fig. 15(b).

6.3. Comparison study

The designed sliding mode controller has weak sensitivity to the parameters which enables it to adapt to voltage fluctuations caused by the PV system. In this section, the characteristics of SMC are compared with PI double-loop controller [6] and Model Predictive Controller (MPC) [29]. This section removes the distributed voltage observer and the SoC balancing control strategy to reliably compare results. Furthermore, the topology of the microgrid is changed to a dyadic circuit to exclude the effect of line impedance on the comparison results, which can be observed in Fig. 16. Without the voltage observer, the bus voltage will deviate from the set point voltage v^{nom} under the droop control, where the constant power load is replaced with resistive loads in the comparison case.

The 1st BESS, 2nd BESS and 3rd BESS are used by SMC designed in Section 3, PI double-loop controller and MPC, respectively. Further, two different sets of parameters are applied to the three types of controllers described above to compare the effect of changes in the parameters.
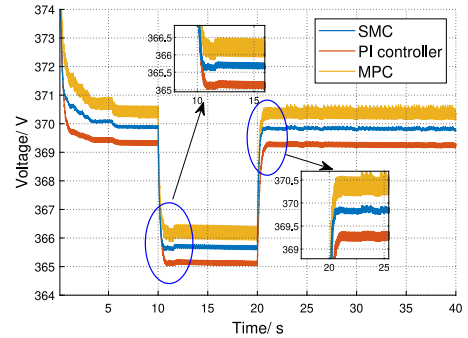

Fig. 17. The compared case for three different controllers.

Detailed parameter information for this section is shown in Table 2, wherein k_p^v/k_i^v and k_p^i/k_i^i denote the proportional/integral factor for the voltage loop and the proportional/integral factor for the current loop, respectively. N_{MPC} and λ_{MPC} denote the prediction horizon and weighting factor for MPC, respectively. It should be reminded that the battery model used for the simulation is not a constant DC source, when replacing the simulation parameters, the change in the initial state will cause a difference in the value of the voltage profile when voltages reach the steady state.

In this case, the simulation time is shortened to 40 s. In the initial stage, the SoC of each BESS is kept consistent to minimize the interference of the SoC balancing control strategy. $Load_2$ and $Load_3$ are connected and disconnected at $t = 10$ s and $t = 20$ s respectively to explore the transient characteristics of the controllers [30,31].
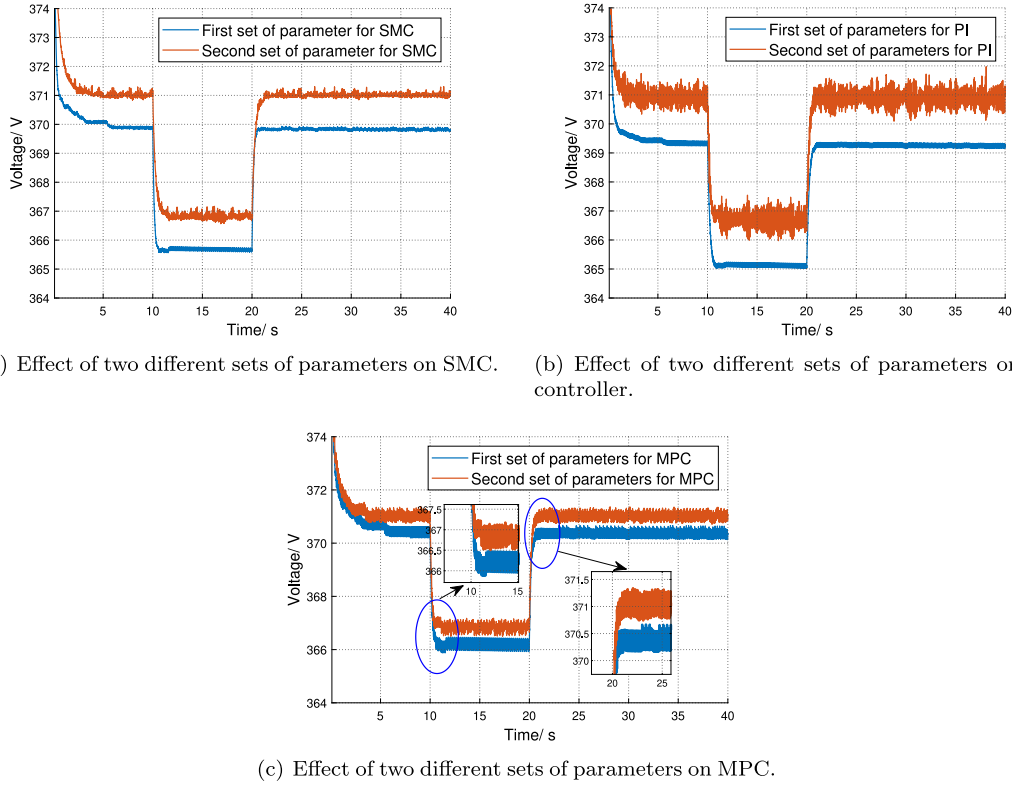
(a) Effect of two different sets of parameters on SMC.

(b) Effect of two different sets of parameters on PI controller.

(c) Effect of two different sets of parameters on MPC.

Fig. 18. Effect of two different sets of parameters on the controllers.

Table 2
Simulation parameters in compared study.

Type	Parameter
Sliding Mode Controller	$\{\alpha_{i,1}, \alpha_{i,2}\} = \{2, 20\}$
PI Controller	$\{k_{p,1}^v, k_{i,1}^v, k_{p,1}^i, k_{i,1}^i\} = \{1.5, 0.8, 1, 0.5\}$
	$\{k_{p,2}^v, k_{i,2}^v, k_{p,2}^i, k_{i,2}^i\} = \{2, 1.5, 1.8, 0.8\}$
Model predictive Controller	$\{N_{MPC,1}, \lambda_{MPC,1}\} = \{3, 0.015\}$
	$\{N_{MPC,2}, \lambda_{MPC,2}\} = \{5, 0.02\}$
Parameters of microgrid	$\{R_b, R_{line}, Load_i\} = \{0.1\ \Omega, (1\ \Omega + 0.001\ H), 40\ \Omega\}$

The simulation results for the three different controllers can be observed in Fig. 17, in which it can be seen by carefully comparing the magnified plots at $t = 10$ s and $t = 20$ s, that the SMC and MPC respond faster during sudden load changes (the SMC and MPC reach a steady state during sudden load changes within 1 s, whereas the PI controller has a response time of about 1.5 s). Meanwhile, the oscillation errors of PI and SMC in reaching a steady state are, obviously, smaller than MPC. Hence, it can be concluded that in this simulation environment, the response speed of SMC and MPC, relative to PI controller, is better; while in terms of steady state error, SMC and PI are significantly better than MPC. Next, the sensitivity of the three controllers to the simulation parameters will be verified.

Keeping the parameters of the microgrid constant and varying the parameters of the three controllers, the simulation results are shown in Fig. 18. It can be seen that the SMC has the lowest sensitivity to the parameters and still maintains high control accuracy and response speed; the PI controller has the highest sensitivity to the parameters due to the more parameters changed (4 parameters in the PI double-loop control); and the MPC is not much affected by the parameters in terms of accuracy. As for the response speed, the MPC response speed under the first set of parameters is faster as the voltage is near 366 V, while the MPC response speed under the second set of parameters is faster as the voltage is near 371 V. This indicates that the MPC response speed for the same parameters may be different at different voltage levels.

In addition, it should be noted that even under the same microgrid parameters, the different initial values lead to different SoC, output currents of the batteries in the BESS under the two sets of control parameters when they reach the steady state, which in turn leads to the difference in the steady state voltage under the droop control. It is a normal phenomenon.

Based on the above analysis, it can be seen that the performance of SMC is less sensitive to the parameters, which follows from (16)–(17), where the control rate is determined only by the positivity/negativity of the sliding mode surface S_i but not the value. The different parameters of MPC have different sensitivities to different voltage levels, which makes it difficult to apply MPC in the context of this study, i.e., microgrids under PV disturbances. The high sensitivity of the PI controller to the parameters is due to the large number of parameters in the dual-loop control and the fact that the existing studies have already concluded through the pole distributions that the stability of the PI controller varies with the input voltage, and it is also difficult to adapt to the PV perturbations.

It should be emphasized that this study has less to discuss about PV operation. In fact, PV is only introduced as a perturbation term, under the existing theory in this paper it can be assumed that the study in this paper is able to be applied to most of the RESs (e.g., wind power systems) which can cause such perturbations. Moreover, compared to the linear system, the nonlinear model developed in this paper has lower complexity, i.e., it is only necessary to know the acceptable power range of each BESS node for the stable operation while it is not necessary to know the topology of the whole microgrid.

7. Conclusion

This study presents a new approach for calculating the equivalent resistance of Battery Energy Storage System, which considers the variability in photovoltaic output by using a nonlinear function for a more accurate representation of the power differences among Battery Energy Storage System. The approach uses a discrete Sliding Mode Controller

to provide better robustness against photovoltaic fluctuations, along with a State of Charge balancing control method that employs sliding mode control to enhance microgrid stability. This control mechanism also ensures uniformity in the State of Charges during charging and discharging cycles. To regulate the mean voltage of each Battery Energy Storage System at the predetermined voltage setpoint, a distributed voltage estimation strategy is used, which resolves the trade-off between State of Charge equilibrium and voltage regulation. The stability of the proposed State of Charge balancing control technique is confirmed by formulating a Lyapunov function. The effectiveness and stability of the control protocol are demonstrated through simulations in MATLAB/Simulink across three different scenarios. Further investigation includes stability control for AC/DC microgrids with unknown topology, and solutions for nonlinear microgrids with various Renewable Energy Sources.

CRediT authorship contribution statement

Boxi Li: Conceptualization, Investigation, Methodology, Writing – original draft, Writing – review & editing. **Tao Huang:** Methodology, Supervision, Writing – review & editing, Investigation, Writing – original draft. **Zhengmin Kong:** Conceptualization, Writing – review & editing, Resources, Investigation. **Lei Chen:** Methodology, Writing – review & editing, Resources. **Jiajia Yang:** Methodology, Writing – review & editing. **Shikuan Sun:** Investigation, Writing – original draft.

Declaration of competing interest

The authors declare that they have no known competing financial interests or personal relationships that could have appeared to influence the work reported in this paper.

Data availability

No data was used for the research described in the article.

Acknowledgments

References

[1] Aftab MA, Hussain SMS, Ikbal Ali I, Ustun TS. Dynamic protection of power systems with high penetration of renewables: A review of the traveling wave based fault location techniques. Int J Elec Power Energy Syst 2020;114.

[2] Popadic B, Dumnic B, Strezoski L. Modeling of initial fault response of inverter-based distributed energy resources for future power system planning. Int J Elec Power Energy Syst 2020;117.

[3] Silveira JPC, Neto PJD, Barros TAD, Ruppert E. Power management of energy storage system with modified interlinking converters topology in hybrid AC/DC microgrid. Int J Elec Power Energy Syst 2021;130.

[4] Sardou IG, Mohsen Zare M, Azad-Farsani E. Robust energy management of a microgrid with photovoltaic inverters in VAR compensation mode. Int J Elec Power Energy Syst 2018;98:118–32.

[5] Yu J, Xia C. Discrete-time capacitor-voltage observer and state-error feedback controller for MMC based on passive theory. Int J Electr Power Energy Syst 2022;117.

[6] Zadeh MK, Gavagsaz-Ghoachani R, Martin JP, Nahid-Mobarakeh B, Pierfederici S, Molinas M. Discrete-time modeling, stability analysis, and active stabilization of DC distribution systems with multiple constant power loads. IEEE Trans Ind Appl 2016;52(6):4888–98.

[7] Mohammadi F, Mohammadi-Ivatloo B, Gharehpetian GB, Ali MH, Wei W, Erdinc O, et al. Robust control strategies for microgrids: A review. IEEE Syst J 2022;16(2):2401–12.

[8] Raeispour M, Atrianfar H, Baghaee HR, Gharehpetian GB. Robust distributed disturbance-resilient H_∞-based control of off-grid microgrids with uncertain communications. IEEE Syst J 2021;15(2):2895–905.

[9] Chaturvedi S, Fulwani D. Adaptive voltage tuning based load sharing in DC microgrid. IEEE Trans Ind Appl 2021;57(1):977–86.

[10] Amirkhan S, Radmehr M, Rezanejad M, Khormali S. A robust control technique for stable operation of a DC/AC hybrid microgrid under parameters and loads variations. Int J Electr Power Energy Syst 2020;117.

[11] Pham TT, Kuo TC, Bui DM. Reliability evaluation of an aggregate battery energy storage system in microgrids under dynamic operation. Int J Elec Power Energy Syst 2020;118.

[12] Yang Y, Xu D, Ma T, Su X. Adaptive cooperative terminal sliding mode control for distributed energy storage systems. IEEE Trans Circuits Syst I, Reg Papers 2021;68(1):434–43.

[13] Zeng Y, Zhang Q, Liu Y, Zhuang X, Lv X, Wang H. An improved distributed secondary control strategy for battery storage system in DC shipboard microgrid. IEEE Trans Ind Appl 2022;58(3):4062–75.

[14] Zeng Y, Zhang Q, Liu Y, Zhuang X, Guo H. Hierarchical cooperative control strategy for battery storage system in islanded DC microgrid. IEEE Trans Power Syst 2022;37(5):4028–39.

[15] Hammad A, Ming Y, Naghmash A, Ammar A, Abdulaziz A. Quick reaching law based global terminal sliding mode control forwind/hydrogen/battery DC microgrid. Appl Energy 2022;316.

[16] Chris G, Gordon R. Algebraic graph theory. Springer-Verlag; 2001, p. 207.

[17] Li B, Yu C, Lu X, Wang F. A novel adaptive droop control strategy for SoC balance in PV-based DC microgrids. ISA Trans 2023;141:351–64.

[18] Wang Z, Li S, Li Q. Continuous nonsingular terminal sliding mode control of DC-DC boost converters subject to time-varying disturbances. IEEE Trans Circuits Syst II, Exp Briefs 2020;67(11):2552–6.

[19] Yu X, Wang B, Galias Z, Chen G. Discretization effect on equivalent control-based multi-input sliding-mode control systems. IEEE Trans Automat Control 2008;53(6):1563–9.

[20] Xu D, Zhang W, Jiang B, Shi P, Wang S. Directed-graph-observer-based model-free cooperative sliding mode control for distributed energy storage systems in DC microgrid. IEEE Trans Ind Informat 2020;16(2):1224–35.

[21] Lu X, Lai J. Distributed cluster cooperation for multiple DC MGs over two-layer switching topologies. IEEE Trans Smart Grid 2020;11(6):4676–87.

[22] Bi K, Sun L, An Q, Duan J. Active SOC balancing control strategy for modular multilevel super capacitor energy storage system. IEEE Trans Power Electron 2021;34(5):4981–92.

[23] Wu H, Chai L, Tian YC. Distributed multirate control of battery energy storage systems for power allocation. IEEE Trans Ind Informat 2022;18(12):8745–54.

[24] Pires VF, Cordeiro A, Foito D, Silva JFA. Dual output and high voltage gain DC-DC converter for PV and fuel cell generators connected to DC bipolar microgrids. IEEE Access 2021;9:157124-157133.

[25] Lin W. DC-DC autotransformer with bidirectional DC fault isolating capability. IEEE Trans Power Electron 2016;31(8):5400–10.

[26] Khalil H. Nonlinear systems (3rd Ed.), 2002.

[27] Michael DP. Graph factors and factorization: 1985–2003: A survey. Discrete Math 2007;307.

[28] Morstyn T, Savkin AV, Hredzak B, Agelidis VG. Multi-agent sliding mode control for state of charge balancing between battery energy storage systems distributed in a DC microgrid. IEEE Trans Smart Grid 2018;9(5):4735–43.

[29] Karami Z, Shafiee Q, Khayat Y, Yaribeygi M, Dragicevic T, Bevrani H. Decentralized model predictive control of DC microgrids with constant power load. IEEE J Em Sel Top P 2021;9(1):451–60.

[30] Zhang Z, Dou C, Yue D, Xue Y, Xie X, et al. Voltage sensitivity-related hybrid coordinated power control for voltage regulation in ADNs. IEEE Trans Smart Grid http://dx.doi.org/10.1109/TSG.2023.3292939.

[31] Bakhshi-Jafarabadi R, Lekic A, Marvasti FD, de Jesus Chavez J, Popov M. Analytical overvoltage and power-sharing control method for photovoltaic-based low-voltage islanded microgrid. IEEE Access 2023;11:134286-297.